14th International Symposium on Turbulence and Shear Flow Phenomena (TSFP14)
Heidelberg, Germany, July 28–31, 2026

TOWARD PREDICTION OF TEMPERATURE ROUGHNESS FUNCTION FOR TURBULENT HEAT TRANSFER OVER ROUGH SURFACES

Yusuke Kuwata, Kuga Terada, Yuki Adachi, Na. Donggeon, Kazuhiko Suga
Department of Mechanical Engineering
Osaka Metropolitan University
1-1, Gakuen-cho, Naka-ku, Sakai 599-8531, Japan
kuwata@omu.ac.jp

ABSTRACT

We performed a series of large eddy simulations (LES) of turbulent heat transfer in a rough-walled open channel with several types of rough surfaces. The aim of this study is to develop a universal predictive model for the temperature roughness function, which quantifies the effects of wall roughness on the mean temperature. We considered 55 irregular rough surfaces with different morphological parameters. The friction Reynolds number was varied among 300, 600, and 900 for each rough surface case, and additional LESs at a friction Reynolds number of 1200 were conducted for selected cases. The results show that the temperature roughness function can be expressed as a function of the roughness Reynolds number and morphological parameters, and that a deep neural network (DNN) successfully models the effects of the morphological parameters on the temperature roughness function. The key parameters affecting the prediction of the temperature roughness function are found to be those related to the slope of surface undulations, namely the effective slope and the effective slope variance. We further develop algebraic correlation models using symbolic regression and find that the proposed correlations provide better predictions not only for the present LES data but also for other rough surfaces reported in the literature, demonstrating broad applicability across different roughness types and Reynolds numbers.

INTRODUCTION

Turbulent heat transfer over rough surfaces is ubiquitous in engineering applications. Familiar examples include turbine blade surfaces and the combustion chambers of internal combustion engines, which become roughened due to deposition, pitting, and erosion of incombustible materials. Surface roughness not only affects the aerodynamic performance of engineering systems but also alters their heat transfer characteristics. For gas turbine blades operating under harsh conditions, roughness-induced enhancement of heat transfer can lead to a significant increase in wall temperature, thereby increasing thermal stress and ultimately reducing the lifespan of the components. This motivates the development of predictive models for turbulent heat transfer over rough surfaces.

A pioneering study on the Stanton number S_t for rough surfaces was conducted by Dipprey & Sabersky (1963), who derived a correlation based on the analogy between the turbulent diffusivities of heat and momentum transfer:

$$S_t = \frac{0.5C_f}{1+\sqrt{0.5C_f}\, g_k(k_s^+, Pr)}, \tag{1}$$

where C_f is the skin-friction coefficient, and $g_k(k_s^+, Pr)$ is a function of the inner-scaled equivalent sand-grain roughness k_s^+ and the Prandtl number Pr, given as follows:

$$g_k(k_s^+, Pr) = A_1 (k_s^+)^m Pr^n + A_2, \tag{2}$$

where A_1, A_2, m, and n are model constants.

The experimental study of close-packed granular roughness by Dipprey & Sabersky (1963) proposed the model constants (A_1,A_2)=(5.19,$-$8.48) and the exponents (m,n)=(0.2,0.44). Other sets of model constants (A_1,A_2), with the exponents (m,n)=(0.2,0.44), have been proposed in subsequent studies Kays & Crawford (1993); Bons (2002); Kuwata (2022*a*). These studies supported the set of exponents (m,n) proposed by Dipprey & Sabersky (1963), although some controversy regarding these exponents remains Li *et al.* (2020); Zhong *et al.* (2023). Another consequence of wall roughness is the modification of the mean temperature profile manifested as a downward shift of the logarithmic mean temperature profile, which is quantified by the temperature roughness function $\Delta\Theta^+$. This is analogous to the velocity roughness function ΔU^+, which represents a downward shift in the logarithmic mean velocity profile and is an important quantity for predicting the mean temperature profile over rough surfaces. The temperature roughness function can be expressed as a function of C_f, S_t, and g_k (Kuwata, 2021). However, determining appropriate values of A_1, A_2, m, and n is challenging because they depend strongly on the morphology of rough surfaces (Kuwata, 2022*a*; Zhong *et al.*, 2023). The goal of this study is to establish a data-driven algebraic model for the model constants A_1 and A_2, while fixing the exponents at (m,n)=(0.2,0.44), by performing large eddy simulations (LESs) of turbulent heat transfer over several types of rough surfaces at different Reynolds numbers.

Methodology

Figure 1 shows a schematic of the rough-walled open-channel flow. The flow was periodic in the streamwise (x) and spanwise (z) directions. The bottom wall was a rough surface while we prescribed the slip boundary conditions for the

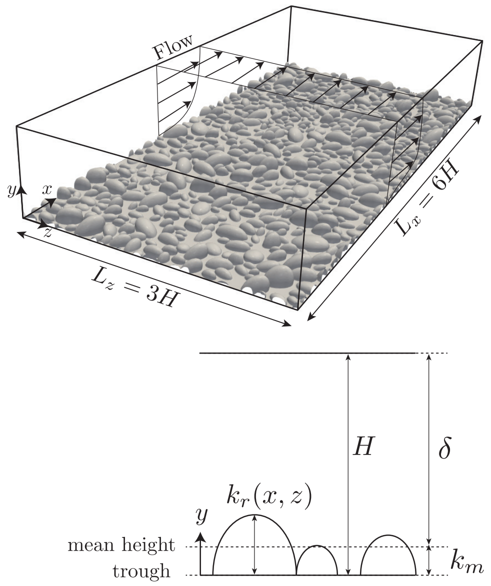

Figure 1. Computational geometry of rough-walled open-channel flow.

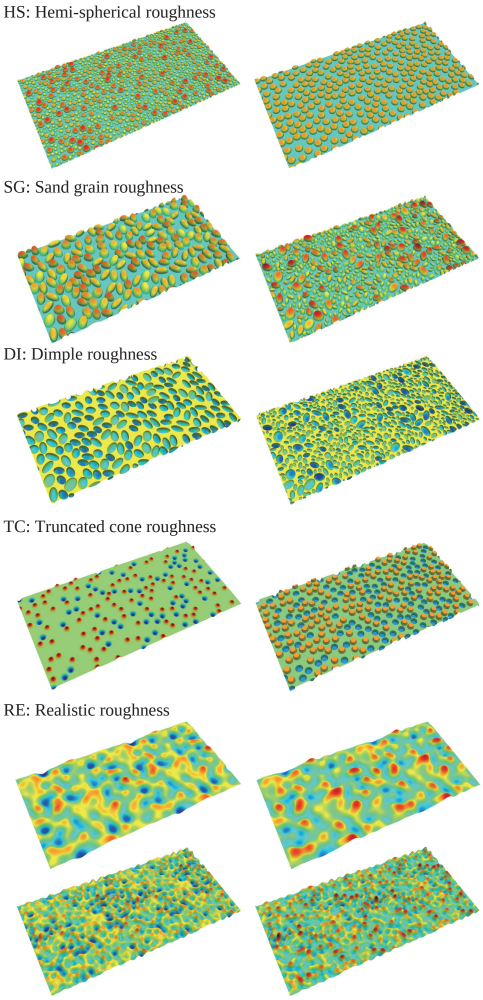

Figure 2. Geometry of rough surfaces: hemi-spherical roughness (case HS), sand-grain roughness (case SG), dimple roughness (case DI), truncated cone roughness (case TC), and realistic roughness (case RE).

top boundary face. The flow was driven by a constant streamwise pressure difference, and the pressure difference was varied such that the friction Reynolds number $Re_\tau = u_\tau \delta/\nu$ was equal to target values of 300, 600, 900, and 1200. Here, u_τ is the friction velocity, and δ is the distance from the mean surface position to the top boundary face. We considered the incompressible fluid with the passive scalar with the Prandtl number of $Pr = 0.7$. We included the uniform internal heat generation in the energy equation to drive the heat transfer. For the thermal boundary conditions, the top boundary face was adiabatic and rough surfaces were isothermally cooled. The LESs were conducted by the double distribution lattice Boltzmann method (LBM) with the wall-adapting local eddy-viscosity model (Ducros *et al.*, 1998). We adopted the 27-velocity multiple-relaxation-time LBM (Suga *et al.*, 2015) for the flow field, while utilizing the 19-velocity regularized LBM (Suga *et al.*, 2017) for the scalar field. The near-wall grid resolution was determined such that the grid spacing in wall units was approximately $\Delta^+ \simeq 2.5$.

We considered five types of rough surfaces: hemi-spherical roughness (HS), sand-grain roughness (SG), dimple (DI), truncated cone (TC), and artificially generated realistic (Re) roughness, as shown in 2. The hemisphere roughness elements or flattened spherical roughness elements with different size were considered for case HS. The SG roughness elements consisted of ellipsoids with a semiaxes ratio of 1.0 : 1.4 : 2.0 with random orientation, which reproduces the hydrodynamic characteristics of sand-grain roughness using a single controlling parameter of the roughness size Scotti (2006). For the dimple (DI) roughness, concave hemi-ellipsoid elements were randomly generated on the reference smooth wall.The truncated cone (TC) roughness is characterized by a cone shape roughness with lower diameter, upper diameter, and height. We considered sharp cones with small truncations as well as the flattened cones with large truncation, and Both pimple- and dimple-type cones were included with different number fractions. Those roughness elements were made at a reference smooth wall of size of $L_x \times L_z$ with random positions and different solidity. In addition to the additive types of roughness (cases HS,SG,DI, and TC), the realistic (RE) artificial roughness was generated using the multi-scale surface generation algorithm in Pérez-Ràfols & Almqvist (2019); Yang *et al.* (2023). The amplitudes and phases of the sinusoidal components were iteratively adjusted such that the probability density function (PDF) and power spectrum (PS) of the height distribution matched the prescribed target profiles. In total, we generated 55 rough surfaces (10 HS, 6 SG, 3 DI, 12 TC, and 24 RE cases) with different morphological characteristics.

For the morphological parameters, we considered the parameters related to the probability density function (PDF) and power spectra (PS) of the surface height elevation, as well as the dimensionless roughness height. The PDF-related parameters under considerations are the skewness factor Sk and kurtosis factor Ku, which are the third and fourth moments of the roughness height elevation, respectively. The energy spectra are reflected by the two slope parameters. One is the effective slope ES, which represents the mean steepness of surface undulations, and the other is the spatial variance of the slope ES_{rms}. Additionally, we considered the non-dimensional height parameter based on the root-mean-square height k_{rms} and the mean peak-to-trough height k_t. Here, k_t is computed by averaging the peak-to-valley height over subdivided surfaces. Figure 3 presents the parameter spaces for the current rough surface samples.

Figure 3 shows the morphological parameter space of the

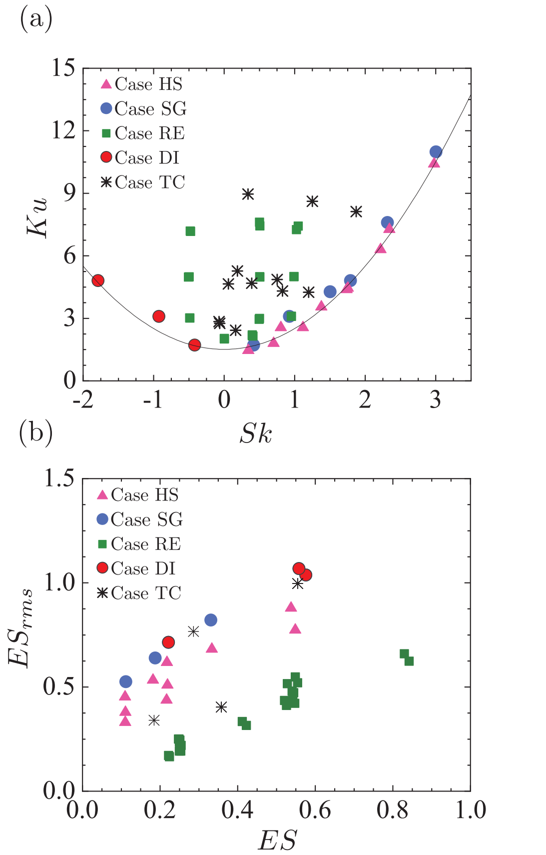

Figure 3. Morphological parameter space: (a) kurtosis factor (*Ku*) against the skewness factor (*Sk*) and (b) spatial variance of the slope ES_{rms} against the effective slope ES. The boundary for the modified Pearson inequality (Klaassen *et al.*, 2000) is included in (a).

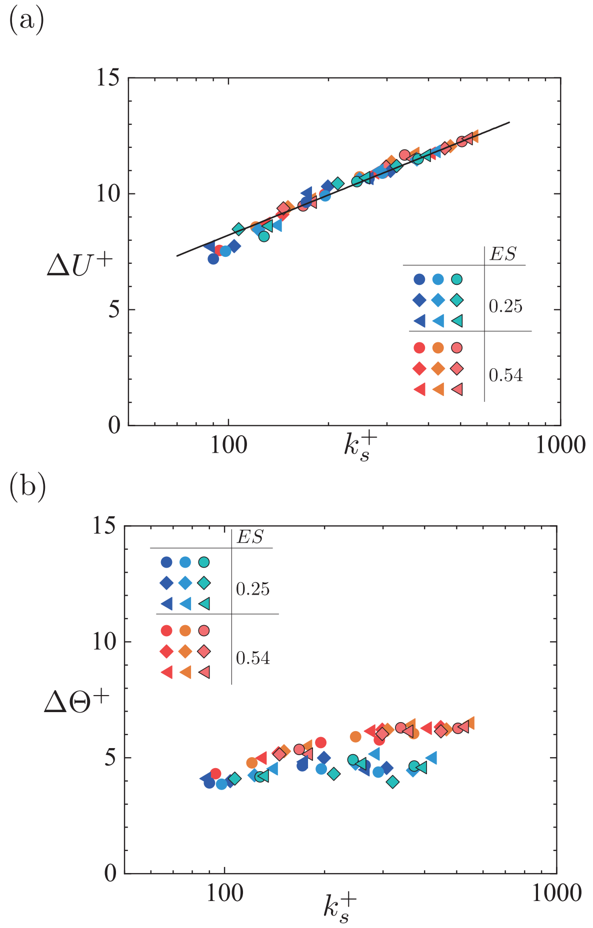

Figure 4. Roughness function against k_s^+ for Re cases: (a) velocity roughness function ΔU^+ and (b) temperature roughness function $\Delta\Theta^+$.

investigated surfaces. The boundary for the modified Pearson inequality (Klaassen *et al.*, 2000), which constrains the possible combinations of *Sk* and *Ku*, is also shown in Figure 3(a).The surfaces consisting purely of pimples (HS and SG) or dimples (DI) were close to this boundary. By contrast, the realistic roughness (RE) and surfaces consisting of truncated pimples and dimples (TC) lie far inside the boundary.The RE surfaces exhibit moderate *Sk* and *Ku*, whereas the HS and SG surfaces give larger positive *Sk* and *Ku* values, which represents the early stages of surface evolution involving sparse deposition, erosion, or pitting. As shown in the *ES* values in Figure 3(b), the present roughness covers from the waviness regime ($ES < 0.35$) to the rough regime ($ES > 0.35$) (Schultz & Flack, 2009). The spatial variation of the slope, quantified by ES_{rms}, is positively correlated with ES, although the correlation between ES_{rms} and ES depends largely on the roughness type; the additive type roughness of cases HS and SG give relatively large ES_{rms}, whereas the RE surfaces yield considerably smaller ES_{rms}.

Results and discussions

To better understand the general trend of the morphological parameters on the temperature roughness function $\Delta\Theta^+$, Fig.4 plots $\Delta\Theta^+$ and ΔU^+ as a function inner-scaled equivalent sand grain roughness k_s^+ for RE rough surfaces where the morphological parameters are systematically varied by controlling the PDF and PS of rough surface height. The temperature roughness function is evaluated as a downward shift value in the logarithmic mean temperature profile with respect to the smooth wall profile at matched Re_τ, and k_s^+ is computed from the velocity roughness function ΔU^+ by using the universal correlation between k_s^+ and ΔU^+ in the fully rough regime Flack *et al.* (2020). We observe from the figure that $\Delta\Theta^+$ is generally lower than ΔU^+, and its trend against k_s^+ is significantly affected by the surface morphology, even in the expected fully rough regime ($k_s^+ > 70$), unlike the trend of ΔU^+. Interestingly, the trend of $\Delta\Theta^+$ in Fig. 4(d) can be grouped into two clusters with different *ES* values. The results in the upper and lower clusters correspond to the cases with higher *ES* values and lower *ES* values, respectively. It is noteworthy that the $\Delta\Theta^+$ exhibits consistent trends in each group despite the fact that the rough surfaces in each group have substantial variation in *Sk*, *Ku*, k_t/k_{rms}. This suggests that the trend of $\Delta\Theta^+$ against k_s^+ is dominantly affected by the slope parameters of *ES* or ES_{rms}.

It is evident from Fig.4 that $\Delta\Theta^+$ is not expressed as a function of k_s^+ solely in the expected fully rough regime ($k_s^+ > 70$) despite that fact that the corresponding velocity roughness function ΔU^+ depends only on k_s^+ irrespective of surface morphology (Flack *et al.*, 2020). To model the trend of $\Delta\Theta^+$ in the fully rough regime, we introduce a following correlation (Kuwata, 2021), which is an extension from the correlation for the Stanton number (Dipprey & Sabersky, 1963):

$$\Delta\Theta^+ = Pr_t\left(\frac{1}{\kappa}\ln(k_s^+) - 8.5\right) + \beta(Pr) - C_1\left((k_s^+)^m Pr^n - C_2\right), \tag{3}$$

where Pr_t is the turbulent Prandtl number, κ is the Karman constant, $\beta(Pr)$ is the log-law intercept for smooth wall turbulence. The last term on the right-hand side of Eq. (3) stands for the departure from the velocity roughness function. Although the results are not shown here, the model with an arbitrary coefficient for C_1 and fixed values for $C_2(=1.8)$ and (m,n)=(0.2,0.44) successfully approximates the trend of $\Delta\Theta^+$ for each roughness case at different Re_τ. This observation motivates us to model the coefficient C_1 as a function of the morphological parameters. However, it is extremely difficult to model the relation between C_1 and the morphological parameters due to the many possible candidates of the morphological parameters such as Sk, Ku, ES, ES_{rms}, and k_t/k_{rms}. In this study, we employ a MLP model to reproduce the complicated relation between the morphological parameters and C_1. The MLP architecture consisted of two hidden layers with 64 and 32 neurons, respectively, and the rectified linear unit (ReLU) activation function was used for the hidden layers. The input is the non-dimensional morphological parameters of Sk, Ku, ES, ES_{rms}, and k_t/k_{rms} and the output is the optimal value of $C1$ determined by the LES results. The supervised dataset was divided into 47 training samples and 5 testing samples, and the number of training epochs was set to 200 to mitigate overfitting. This investigation aims to identify the key parameters that dominantly affect the prediction of $\Delta\Theta^+$. Hence, we performed a sensitivity analysis by varying the combinations of the input parameters. We trained 1000 MLP models using random selections of the training and testing subsets, and the MSEs of the test data for the 1000 MLP models were averaged.

To explore the effects of the choice of the input parameters on the predictive performance, Figure 5 presents the ensemble-averaged MSE for predicting C_1 by varying the combination of the input parameters. As expected, the MSE generally decreases as the number of input parameters increases. More importantly, the MLP models that exclude ES or ES_{rms} (model No.25-31) have a poor prediction with relatively larger MSE values, suggesting that the slope parameters, namely the ES or ES_{rms}, are the key parameters that affect the prediction of the model coefficient C_1 for $\Delta\Theta^+$. Notably, the model with two input parameters of ES and ES_{rms} (model No.1) gives the best prediction, indicating the importance in those parameters for predicting $\Delta\Theta^+$. This supports the previous observation from Fig.4 that the trend of $\Delta\Theta^+$ against k_s^+ strongly depends on ES. To obtain physical understanding of the effects of ES and ES_{rms}, we attempt to interpret the black box DNN model with ES and ES_{rms} by analyzing accumulated local effects (ALE) plots, which visualizes the average effect of the input parameters on the prediction. Although the results are not shown here, the ALE plots confirm the decreasing trend of C_1 with ES and ES_{rms} although the trends saturate above the threshold values of $ES \simeq 0.4$ and $ES_{rms} \simeq 0.8$. The decreasing trend of C_1 against ES and ES_{rms} means that $\Delta\Theta^+$ tends to be lower for surfaces with smaller ES and ES_{rms} values. Interestingly, this is consistent with the observation from $\Delta\Theta^+$ in Fig.4 and also supports the DNS results for sinusoidal rough surfaces by Kuwata *et al.* (2024) who showed that the wavy surfaces with smaller steepness yields smaller $\Delta\Theta^+$.

Motivated by the previous finding that ES and ES_{rms} serve as the two key parameters for predicting C_1, we develop an algebraic model for C_1 based solely on these quantities. In

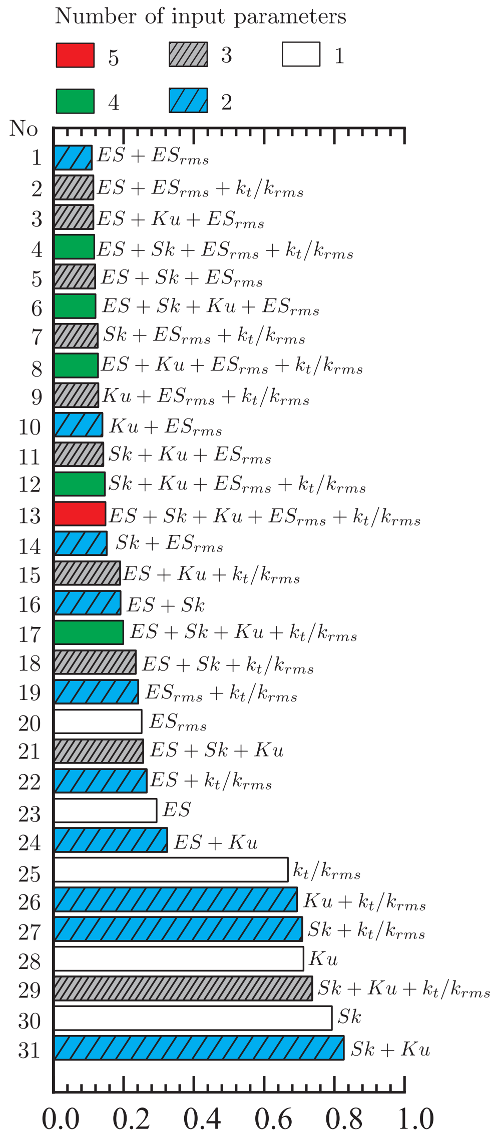

Figure 5. Mean square error of the MLP models with different combinations of input parameters.

this study, symbolic regression is employed to construct the predictive model. This approach does not require any predefined assumptions regarding the functional form and is capable of identifying an optimal mathematical expression. For symbolic regression, we use the open-source library PySR, which is based on a multi-population evolutionary algorithm inspired by biological evolution. Although this method can automatically identify the key parameters from a given set of inputs, we restrict the input parameters to derive a simple model with robust predictive capability across a wide range of rough surfaces. Specifically, only ES and ES_{rms} are used as input parameters, as they dominantly influence C_1. Here, we present the predictive performance of the model based on ES:

$$C_1 = \exp(1.59 - ES). \tag{4}$$

Figure 6(a) assesses the predictive performance of $\Delta\Theta^+$ for all 170 cases. The model incorporating ES exhibits better predictive performance, with a mean squared error (MSE) of 0.176, which is comparable to that of the machine-learning model shown in Fig. 5. We next examine the capability of the proposed model to predict $\Delta\Theta^+$ for unseen external datasets,

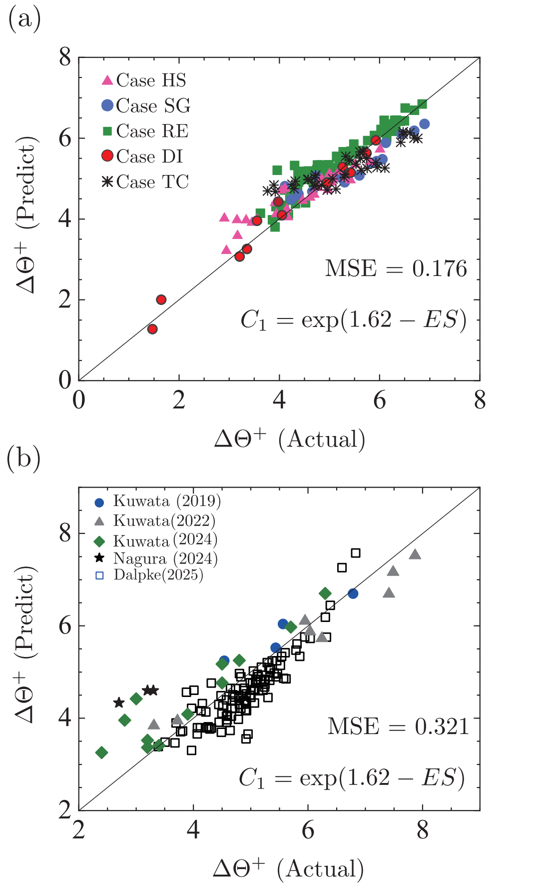

Figure 6. Predictive performance of the proposed model: (a) prediction of $\Delta\Theta^+$ for the present LES data and (b) prediction of $\Delta\Theta^+$ for the external dataset from Kuwata (2021, 2022*b*); Kuwata *et al.* (2024); Nagura *et al.* (2024); **?**

including DNS data for: (i) irregular rough surfaces with different morphological parameters at $Re_\tau = 800$ (**?**); (ii) peak-dominated irregular surfaces at different Re_τ, ranging from $k_s^+ = 32$ to 694 (Kuwata, 2022*b*); (iii) systematically varied irregular surfaces at $Re_\tau = 450$ (Kuwata, 2021); (iv) three-dimensional regular sinusoidal roughness at different Re_τ and wavelengths (Kuwata *et al.*, 2024); and (v) three-dimensional regularly distributed hemispheres at $Re_\tau = 660$ (Nagura *et al.*, 2024). Figure 6(b) shows the predictive performance of the proposed C_1 model incorporating ES for $\Delta\Theta^+$, demonstrating reasonable accuracy across several types of roughness. The MSE of the proposed model is 0.321, which is considerably smaller than those of existing models: 4.4 for Dipprey & Sabersky (1963) with $(C_1, C_2) = (5.19, 1.64)$ and 2.3 for Kays & Crawford (1993) with $(C_1, C_2) = (1.0, 0.0)$. These results indicate that the proposed ES-aided algebraic model exhibits broader applicability across different roughness types and Reynolds numbers compared with existing empirical models.

CONCLUSION

A series of large eddy simulations (LES) of turbulent heat transfer in a rough-walled open channel are performed for several types of rough surfaces at different friction Reynolds numbers. Using the LES dataset, we develop a universal predictive model for the temperature roughness function, which quantifies the effects of wall roughness on the mean temperature. We consider five types of roughness: hemispherical roughness, sand-grain roughness, dimple roughness, truncated-cone roughness, and realistic irregular roughness, and generate a total of 55 rough surfaces with different morphological parameters. The friction Reynolds number is varied among 300, 600, and 900 for each roughness case, and additional simulations at $Re_\tau = 1200$ are conducted for selected cases. The LES results for realistic roughness show that the temperature roughness function can be modeled as a function of the roughness Reynolds number and slope-based parameters, namely the effective slope and slope variance. Specifically, the temperature roughness function, when plotted against the equivalent sand-grain roughness, tends to decrease with decreasing slope-based parameters. This trend is supported by a sensitivity analysis using a multi-layer perceptron model, which indicates that slope-based parameters are key factors governing the prediction of the temperature roughness function. We further develop an algebraic correlation using symbolic regression and find that incorporating the effective slope provides improved predictions not only for the present LES data but also for other rough surfaces reported in the literature, demonstrating broad applicability across different roughness types and Reynolds numbers.

Acknowledgments

The authors extend their heartfelt gratitude to their colleague, Dr. M. Kaneda, for invaluable support. The authors gratefully acknowledge Mr. Simon Dalpke and Dr. Alexander Stroh at the Karlsruhe Institute of Technology for providing the data used in this study. This study was partially funded by a grant (No. 21H01266) from the Japan Society for the Promotion of Science (JSPS). The numerical calculations were carried out on the TSUBAME4.0 supercomputer at Tokyo Institute of Technology in research projects (ID: hp250033).

REFERENCES

Bons, J. P. 2002 St and Cf augmentation for real turbine roughness with elevated freestream turbulence. In *ASME Turbo Expo 2002: Power for Land, Sea, and Air*, pp. 349–363. American Society of Mechanical Engineers.

Dipprey, DF & Sabersky, RH. 1963 Heat and momentum transfer in smooth and rough tubes at various prandtl numbers. *Int. J. Heat Mass Transfer* **6** (5), 329–353.

Ducros, F, Nicoud, F & Poinsot, T 1998 Wall-adapting local eddy-viscosity models for simulations in complex geometries. *Numerical Methods for Fluid Dynamics VI* **6**, 293–299.

Flack, K.A., Schultz, M.P. & Barros, J.M. 2020 Skin friction measurements of systematically-varied roughness: Probing the role of roughness amplitude and skewness. *Flow, Turb. Combust.* **104** (2), 317–329.

Kays, WM & Crawford, ME 1993 *Convective Heat and Mass Transfer, 3rd Edition*. McGraw-Hill, New York, NY.

Klaassen, CAJ, Mokveld, PJ & Van Es, Bert 2000 Squared skewness minus kurtosis bounded by 186/125 for unimodal distributions. *Statistics & probability letters* **50** (2), 131–135.

Kuwata, Y. 2021 Direct numerical simulation of turbulent heat transfer on the reynolds analogy over irregular rough surfaces. *Int. J. Heat Fluid Flow* **92**, 108859.

Kuwata, Y 2022*a* Reynolds number dependence of turbulent heat transfer over irregular rough surfaces. *Phys. Fluids* **34** (4).

Kuwata, Y. 2022*b* Reynolds number dependence of turbulent heat transfer over irregular rough surfaces. *Phys. Fluids* **34** (4), 045118.

Kuwata, Y, Yagasaki, W & Suga, K 2024 Effects of steepness on turbulent heat transfer over sinusoidal rough surfaces. *Int. J. Heat Fluid Flow* **109**, 109537.

Li, Q.i., Bou-Zeid, E., Grimmond, S., Zilitinkevich, S. & Katul, G. 2020 Revisiting the relation between momentum and scalar roughness lengths of urban surfaces. *Q. J. Roy. Meteor. Soc.* **146** (732), 3144–3164.

Nagura, R, Suga, K & Kuwata, Y 2024 Direct numerical simulation of turbulent heat transfer over surfaces with hemisphere protrusions. *Results in Engineering* **24**, 103284.

Pérez-Ràfols, F & Almqvist, A 2019 Generating randomly rough surfaces with given height probability distribution and power spectrum. *Tribology International* **131**, 591–604.

Schultz, M. P. & Flack, K. A. 2009 Turbulent boundary layers on a systematically varied rough wall. *Phys. Fluids* **21** (1), 015104.

Scotti, A 2006 Direct numerical simulation of turbulent channel flows with boundary roughened with virtual sandpaper. *Phys. Fluids* **18** (3).

Suga, K, Chikasue, R & Kuwata, Y. 2017 Modelling turbulent and dispersion heat fluxes in turbulent porous medium flows using the resolved LES data. *Int. J. Heat Fluid Flow* **68**, 225–236.

Suga, K, Kuwata, Y, Takashima, K & Chikasue, R 2015 A D3Q27 multiple-relaxation-time lattice Boltzmann method for turbulent flows. *Comput. Math. Appl.* **69** (6), 518–529.

Yang, J., Velandia, J., Bansmer, S., Stroh, A. & Forooghi, P. 2023 A comparison of hydrodynamic and thermal properties of artificially generated against realistic rough surfaces. *Int. J. Heat Fluid Flow* **99**, 109093.

Zhong, K., Hutchins, N. & Chung, D. 2023 Heat-transfer scaling at moderate Prandtl numbers in the fully rough regime. *J. Fluid Mech.* **959**, A8.